Systems/Circuits

Physiological Properties of Neurons in Bat Entorhinal Cortex Exhibit an Inverse Gradient along the Dorsal–Ventral Axis Compared to Entorhinal Neurons in Rat

James G. Heys,[1] Christopher F. Shay,[1] Katrina M. MacLeod,[3] Menno P. Witter,[5] Cynthia F. Moss,[4] and Michael E. Hasselmo[1,2]

[1]Graduate Program for Neuroscience and [2]Department of Psychological and Brain Sciences, Center for Systems Neuroscience, Boston University, Boston, Massachusetts 02215, Departments of [3]Biology and [4]Psychology, University of Maryland, College Park, Maryland 20742, and [5]Kavli Institute for Systems Neuroscience & Centre for Neural Computation, Faculty of Medicine, Norwegian University of Science and Technology, Trondheim 7491, Norway

Medial entorhinal cortex (MEC) grid cells exhibit firing fields spread across the environment on the vertices of a regular tessellating triangular grid. In rodents, the size of the firing fields and the spacing between the firing fields are topographically organized such that grid cells located more ventrally in MEC exhibit larger grid fields and larger grid-field spacing compared with grid cells located more dorsally. Previous experiments in brain slices from rodents have shown that several intrinsic cellular electrophysiological properties of stellate cells in layer II of MEC change systematically in neurons positioned along the dorsal–ventral axis of MEC, suggesting that these intrinsic cellular properties might control grid-field spacing. In the bat, grid cells in MEC display a functional topography in terms of grid-field spacing, similar to what has been reported in rodents. However, it is unclear whether neurons in bat MEC exhibit similar gradients of cellular physiological properties, which may serve as a conserved mechanism underlying grid-field spacing in mammals. To test whether entorhinal cortex (EC) neurons in rats and bats exhibit similar electrophysiological gradients, we performed whole-cell patch recordings along the dorsal–ventral axis of EC in bats. Surprisingly, our data demonstrate that the sag response properties and the resonance properties recorded in layer II neurons of entorhinal cortex in the Egyptian fruit bat demonstrate an inverse relationship along the dorsal–ventral axis compared with the rat.

Key words: **entorhinal cortex; grid cell; *h* current**

Significance Statement

As animals navigate, neurons in medial entorhinal cortex (MEC), termed grid cells, discharge at regular spatial intervals. In bats and rats, the spacing between the firing fields of grid cells changes systematically along the dorsal–ventral axis of MEC. It has been proposed that these changes could be generated by systematic differences in the intrinsic cellular physiology of neurons distributed along the dorsal–ventral axis of MEC. The results from our study show that key intrinsic physiological properties of neurons in entorhinal cortex of the bat and rat change in the opposite direction along the dorsal–ventral axis of entorhinal cortex, suggesting that these intrinsic physiological properties cannot account in the same way across species for the change in grid-field spacing shown along the dorsal–ventral axis.

Introduction

Neurons in medial entorhinal cortex (MEC), termed grid cells, fire selectively when an animal traverses spatial locations arranged on the vertices of a triangular lattice (Fyhn et al., 2004; Hafting et al., 2005). Grid cells have been observed across a wide range of mammalian species including rats, mice, bats, nonhu-

Received May 7, 2015; revised March 4, 2016; accepted March 8, 2016.

Author contributions: J.G.H., K.M.M., C.F.M., and M.E.H. designed research; J.G.H., C.F.S., and M.P.W. performed research; J.G.H. and M.P.W. analyzed data; J.G.H., K.M.M., M.P.W., C.F.M., and M.E.H. wrote the paper.

This work was supported by Office of Naval Research Multidisciplinary University Research Initiative N00014-10-1-0936 to M.E.H. and ONR N000141210339 to C.F.M. We thank Nachum Ulanovsky (Weizmann Institute) and Walter Metzner (UCLA) for shipping the Egyptian fruit bats to us for these experiments, and Catherine Carr, Matthew Roesch, Mark Sheffield, and Wei Xian for technical support and helpful discussions.

The authors declare no competing financial interests.

Correspondence should be addressed to either Dr. James Heys or Michael E. Hasselmo, Boston University, 2 Cummington Street, Boston, MA 02215. E-mail: james.heys@northwestern.edu or hasselmo@bu.edu.

J. G. Heys' present address: Department of Neurobiology, Northwestern University, 2205 Tech Drive, Evanston, IL, 60208.

C. F. Moss' present address: Departments of Psychological and Brain Sciences and Neuroscience, Johns Hopkins University, Baltimore, MD 21218.

DOI:10.1523/JNEUROSCI.1791-15.2016

 0270-6474/16/364591-09$15.00/0

man primates and humans (Hafting et al., 2005; Fyhn et al., 2008; Doeller et al., 2010; Yartsev et al., 2011; Killian et al., 2012; Jacobs et al., 2013). The seemingly conserved neural representation in MEC grid cells across this wide range of species raises the question whether there could be an underlying neural mechanism that is also conserved across these species.

Although the mechanism(s) generating the grid cell response remain largely unknown, advances have come from an interaction between electrophysiological experiments conducted in the behaving animal and in slice preparations. Recordings demonstrate that grid-field spacing increases in grid cells located more ventrally in MEC in both the foraging rat (Hafting et al., 2005; Stensola et al., 2012) and in the crawling Egyptian fruit bat (Yartsev et al., 2011). In the rodent, these differences in grid-field spacing coincide with systematic differences in the intrinsic cellular physiology displayed among neurons at different dorsal–ventral positions (Giocomo et al., 2007; Garden et al., 2008; Giocomo and Hasselmo, 2009; Boehlen et al., 2010; Pastoll et al., 2012; Shay et al., 2012), suggesting that intrinsic cellular physiology may underlie grid-field spacing. For example, layer II stellate cells in the rodent MEC display a large amplitude sag response and a bandpass-shaped impedance profile at membrane potentials near rest due to the expression of the hyperpolarization activated, cyclic nucleotide gated cation current (HCN; *h* current; Alonso and Klink, 1993; Dickson et al., 2000; Erchova et al., 2004; Nolan et al., 2007). Rodent stellate cells located in dorsal MEC exhibit faster *h* current time constants and higher peak membrane potential resonance frequency than stellate cells located in ventral MEC, which could be attributed to differential HCN subunit expression along the dorsal–ventral axis of MEC (Giocomo et al., 2007; Giocomo and Hasselmo, 2008, 2009). Furthermore, grid-cell recordings from HCN1 knock-out mice show a significant increase in grid-field spacing and grid-field size compared with wild-type mice (Giocomo et al., 2011). Given the similar functional dorsal–ventral gradient of grid cell spacing observed in rodents and Egyptian fruit bats and the physiological gradient in the rodent that could serve as the mechanism underlying the functional gradient, we addressed whether bats also exhibit a similar physiological gradient. If so, this would point to a conserved mechanism underlying grid-field spacing. Remarkably, our data demonstrate that the sag response properties and the peak membrane potential resonance frequency recorded in layer II neurons of entorhinal cortex in the bat have an inverse relationship along the dorsal–ventral axis compared with that in the rat.

Materials and Methods

Slice preparation. Horizontal sections (400 μm thick) were made from 17 male and female Egyptian fruit bats (*Rousettus aegyptiacus*) and seven juvenile (P17–P20) male Long–Evans rats. The Egyptian fruit bats ranged in age approximately from 6 months to 4 years and ranged in weight from 80 to 160 g. Note that physiological measurements made in the juvenile rodent are similar from P17 into adulthood (Boehlen et al., 2010). Similar to rats, the body temperate of Egyptian fruit bats is ~37°C (Noll, 1979). All procedures were in accordance with the Institutional Animal Care and Use Committee of the University of Maryland, College Park, and Boston University. Immediately after decapitation, the brain was removed from the skull and placed in oxygenated 4°C artificial CSF (ACSF) with the following concentrations (in mM): 130 NaCl, 3 KCl, 2 $MgCl_2$, 26 $NaHCO_3$, 2 $CaCl_2$, 1.25 NaH_2PO_4, 3 HEPES, and 12 dextrose. The osmolarity of the ACSF was adjusted to be within a range of 305–325 mOsm. Brains were rapidly extracted in cold ACSF, blocked, and sectioned (Leica VT1000S). The sections were then incubated for 30 min at 31°C, followed by another 30 min incubation period at room temperature. For all bat recordings, a modified incubation solution was used in which NaCl was replaced with 130 mM *N*-methyl-D-glutamine (NMDG). Slices were incubated in the NMDG solution for 12 min immediately after sectioning, and were subsequently transferred to normal ACSF recording solution for the remainder of the incubation period. NMDG incubation solution was used to improve slice health in the adult bat recordings. Incubation in NMDG was not used for the juvenile rat slices, as washout is difficult in juvenile tissue, which impedes Giga-seals (Ting et al., 2014). Aside from slice health in the adult tissue, the NMDG incubation solution does not produce any known changes in the cellular electrophysiology (Heys et al., 2013). Synaptic blockers were not used during any of the recordings. The same recording solutions and equipment were used during experiments in both species and experiments in both species were interleaved across days to ensure that recording conditions were consistent.

Electrophysiological recordings. Three to 6 MΩ borosilicate glass patch pipettes were made using a Sutter P-97 pipette puller and filled with internal recording solution with the following concentrations (in mM): 110 K-gluconate, 20 KCl, 1 EGTA, 2 $MgCl_2$, 10 HEPES, 2 Na_2ATP, 0.3 Na_2GTP, 10 phosphocreatine, and 0.1% biocytin. After incubation, individual slices were placed in a 20 series holding chamber (Warner Instrument) and bathed in 37°C oxygenated ACSF. Pipette capacitance and bridge balance compensation was made using a Multiclamp 700B amplifier (Molecular Devices). The data were low-pass filtered at 10 kHz, digitized using a National Instruments board and sampled at a rate of 30 kHz using custom written IGOR Pro acquisition software. All recordings were not corrected for the liquid junction potential, which was measured to be 6 mV (MacLeod et al., 2007).

Whole-cell patch-clamp recordings were made from 58 layer II neurons in entorhinal cortex of the Egyptian fruit bat and 24 layer II neurons in entorhinal cortex of the rat. Neurons were visually identified using a differential interference contrast microscope and confirmed to be layer II cells based on the proximity to the superficial edge of the horizontal slice (see Fig. 2*B*). Neuronal morphology of the layer II neurons was identified using biocytin staining and imaged according to procedures outlined by Giocomo et al. (2007) and MacLeod et al. (2007). Recordings in layer II neurons from the rat were confirmed to be stellate cells based on their morphology and characteristic electrophysiological profile (Alonso and Llinás, 1989; Alonso and Klink, 1993; Klink and Alonso, 1997).

Data analysis. All data were analyzed using MATLAB (v11a). Sag response was generated using a 3 s hyperpolarizing current step. DC holding current was applied to step the neuron from −60 to −80 mV. The sag ratio was computed as the difference between the initial peak voltage after the hyperpolarizing current step and the steady-state voltage after the hyperpolarizing current step, divided by the difference between the initial voltage and the initial peak voltage after the hyperpolarizing current step. The sag time constant (τ_{sag}) was fitted with an exponential of the form:

$$V_m(t) = A_1 e^{-t/\tau_{sag}} + A2,$$

where V_m is membrane potential, A_1 and A_2 are constants. The membrane time constant was fit using a single exponential function, during a 75 ms response to the current injection starting from the onset of the hyperpolarizing current step. The impedance function was generated using a sinusoidal current injection that increased linearly in frequency from 0 to 20 Hz over 20 s. The impedance profile was computed as the fast Fourier transform of the voltage response divided by the fast Fourier transform of the injected current. The resonance frequency was measured by fitting the impedance function with a polynomial and finding the frequency that occurred at the maximum of the curve. The resonance strength was computed using the polynomial fit as the ratio of amplitude of the impedance profile at the resonance frequency divided by the amplitude of the impedance profile at the *y*-intercept.

Anatomical measurements. After horizontal slices were cut the remaining nonsectioned brain was fixed in 4% paraformaldehyde in 0.1 M PBS for 2–5 d. Brains were then transferred to a 30% sucrose solution in 0.1 M PBS until the brains sank in the solution (~1.5 d). Using a freezing microtome, 50 μm sagittal sections were cut from the remaining brain

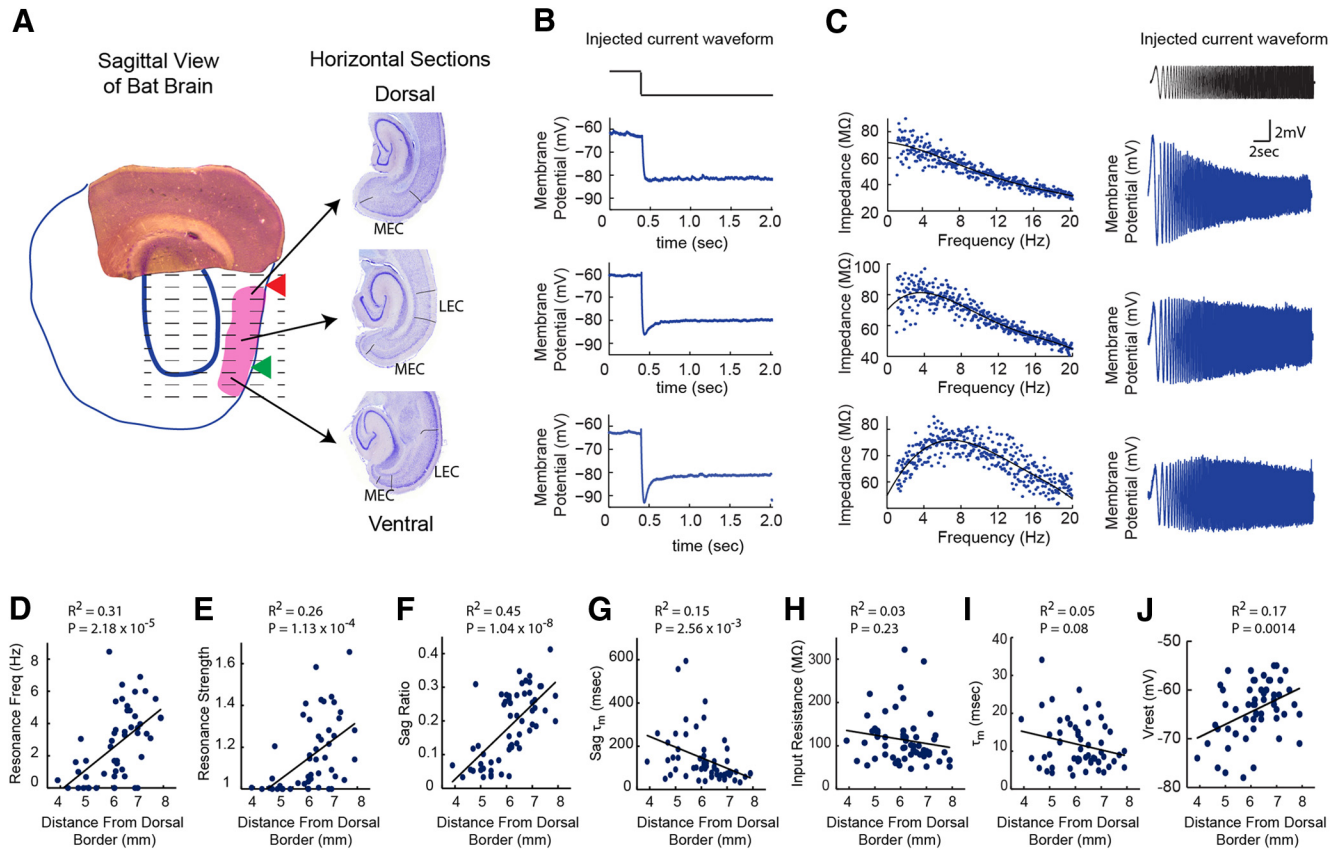

Figure 1. Whole-cell recordings across the dorsal–ventral axis of EC in the Egyptian fruit bat. ***A***, Image depicts shape and range of horizontal slices taken from a dorsal level through EC (top, right), a middle level along the dorsal–ventral axis of EC (middle, right), and ventral level around the border between MEC and the lateral EC (LEC; bottom, right). Red and green arrows mark the dorsal and ventral border of MEC. The sagittal section (top, left) is an image taken from the remaining tissue that was not used for horizontal recording sections. The magenta region depicts approximate location of EC. ***B***, ***C***, Example traces depicting the sag response (***B***) and the impedance profile (***C***) from the dorsal region of EC (top), the middle point along the dorsal–ventral axis of EC (middle), and the ventral region of EC (bottom). ***D***, Resonance frequency, (***E***) resonance strength, (***F***) sag ratio, (***G***) sag time constant, (***H***) input resistance, (***I***) membrane time constant, and (***J***) resting membrane potential measured in neurons located along the dorsal–ventral axis of EC. R^2 and p values are shown for linear fits.

and the sections were stained with cresyl violet. To standardize the anatomical measurements of each recording across bat brains the sagittal sections were aligned to a common reference image. The position of each horizontal recording slice could then be reconstructed by accounting for the thickness of each recording section (400 μm) and its order in the series of horizontal sections, and aligning the series of horizontal recording sections below the sagittal section (see Fig. 2*A*). The distance from the dorsal surface of the brain was then measured to the midpoint of each horizontal recording slice to obtain the dorsal–ventral position of each recording. After recording, the 400-μm-thick horizontal sections were transferred to 4% paraformaldehyde in 0.1 M PBS for 2–5 d. These sections were subsequently incubated for 1 h in a 70 μM DAPi solution in DDH_2O and imaged using epifluorescence microscopy to demonstrate the characteristic shape of the hippocampus and parahippocampal regions at each dorsal–ventral position. As further confirmation of the anatomical location, the thick recording sections were compared with a series of horizontal histological sections (50 μm) that was made across the entire dorsal–ventral axis and stained using cresyl violet (see Fig. 2*A*).

Results

In horizontal brain slices of the Egyptian fruit bat, *R. aegyptiacus*, we performed whole-cell patch-clamp recordings from layer II neurons at positions spanning the dorsal–ventral extent of entorhinal cortex (EC), including MEC and the ventral aspect of lateral entorhinal which is located ventral to MEC. This work extends our previous whole-cell study of MEC layer II neurons in the big brown bat, *Eptesicus fuscus*, to include the same bat species used to map grid cells (Yartsev et al., 2011). The brain of *R. aegyptiacus* is ~8–10 times larger than that of *E. fuscus*, which allowed a systematic study of cells along the dorsal–ventral axis of EC. The dorsal–ventral location of each recording was determined using anatomical reconstructions of each brain (Figs. 1*A*, 2). Consistent with our previous findings from the big brown bat (Heys et al., 2013), there were layer II neurons in EC of the Egyptian fruit bat that exhibited morphological properties similar to layer II stellate cells and fan cells found across the dorsal–ventral extent of EC in the rat (Fig. 2*B*). Individual recordings of these neurons in the Egyptian fruit bat displayed different sag responses and impedance profiles at different positions along the dorsal–ventral axis of EC (Fig. 1*A–C*). Specifically, across the population of layer II bat neurons in the Egyptian fruit bat, the resonance frequency ($n = 52$), resonance strength ($n = 52$), and sag ratio ($n = 58$) significantly increased in neurons located at more ventral positions in EC ($p < 0.01$ for all 3 measures, Spearman test; Fig. 1*D–F*). Consistent with this, the sag activation time constant significantly decreased in bat neurons located at more ventral positions in EC ($p < 0.01$, $n = 58$, Spearman Test) (Fig. 1*G*). In addition, when measuring the sag response and impedance profile across multiple cells within each bat the same trends were observed (Fig. 3). Although there was a trend toward higher input resistance among neurons in the Egyptian fruit bat located more dorsally in EC, this trend was not significant ($p = 0.06$, $n = 58$, Spearman test; Fig. 1*H*). Recordings on the membrane time constant did not show a significant change along the dorsal–

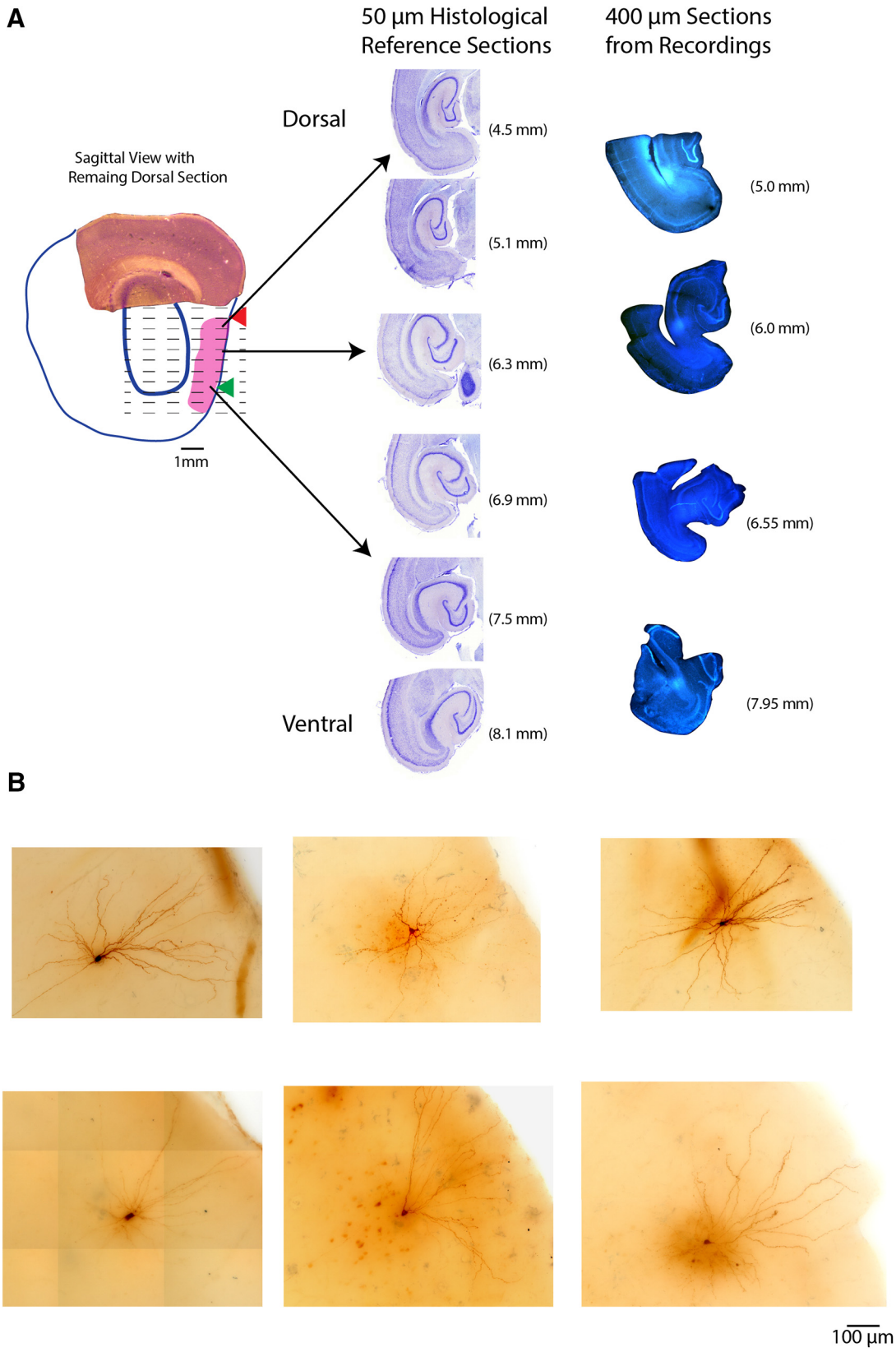

Figure 2. Histological sections from EC of the Egyptian fruit bat. ***A***, Sagittal section with diagram (left) shows the remaining dorsal brain that was not sectioned for recordings. Dashed lines indicate 400 μm horizontal sections that were made for physiological recordings. Red and green arrows mark the dorsal and ventral border of MEC. The magenta region depicts approximate location of EC. Thin horizontal 50 μm sections stained with cresyl violet (middle) were used to confirm dorsal–ventral locations of the thick horizontal recording sections. Four-hundred micrometer horizontal recordings sections (right) from a single bat are shown in series from the dorsal aspect of EC (top) to the ventral aspect of EC (bottom). Blue sections are stained with DAPi. Depth from the dorsal border of the sagittal section shown on the left is shown in parenthesis. Note the consistent changes in the shape of the dentate gyrus from dorsal to ventral in both the reference horizontal sections (middle) and the recording sections (right). ***B***, Example of six recorded neurons from the bat, filled with biotin and stained with DAB.

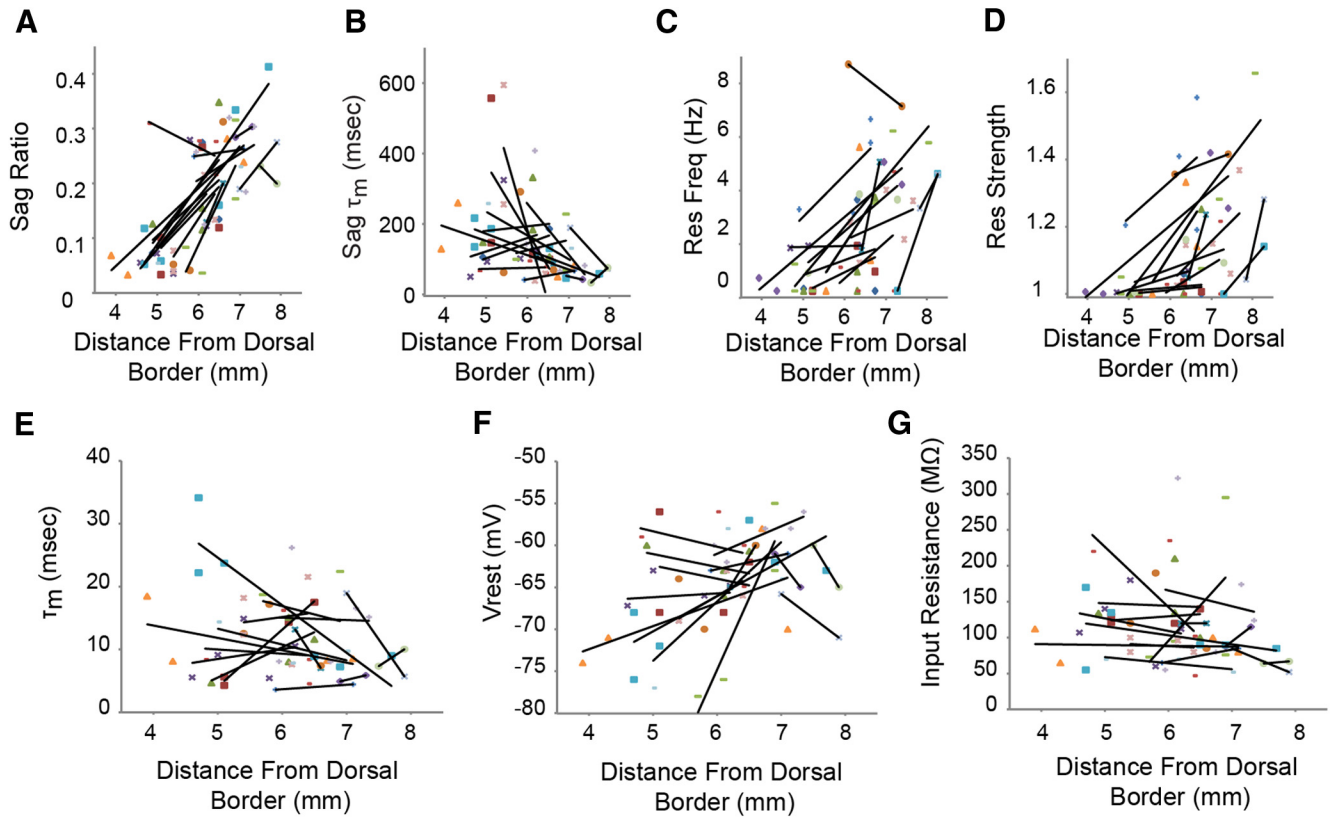

Figure 3. Whole-cell recordings within bat. ***A***, Sag ratio, (***B***) sag time constant, (***C***) resonance frequency, (***D***) resonance strength, (***E***) membrane time constant input resistance, (***F***) resting membrane potential, and (***G***) input resistance measured in neurons located along the dorsal–ventral axis of EC for each bat. Data points within each individual bat are linked by black lines.

ventral axis ($p = 0.25$, $n = 58$, Spearman test) (Fig. 1*I*), whereas resting membrane potential did show a significant trend along the dorsal–axis (Fig. 1*J*; $p < 0.01$, $n = 58$, Spearman test).

In rodent layer II stellate cells, the large amplitude sag response and bandpass shaped impedance profile at membrane potentials near rest arise from the expression of *h* current (Alonso and Klink, 1993; Dickson et al., 2000; Erchova et al., 2004; Nolan et al., 2007). Our results demonstrate that in layer II neurons of the Egyptian fruit bat, the sag response could be nearly abolished through application of selective *h*-current blocker ZD 7288 (10 μM; Fig. 4*A*). The mean sag ratio measured across five neurons was 0.25 ± 0.06 and 0.04 ± 0.01 after bath application of ZD 7288 ($p < 0.01$; paired Student's *t* test; Fig. 4*A*, right). Similarly, the bandpass impedance profile in layer II neurons in the bat was completely abolished using 10 μM ZD 7288 (Fig. 4*B*). The mean resonance frequency across five neurons was 3.49 ± 0.83 Hz before and 0 ± 0 Hz after bath application of ZD 7288 ($p < 0.01$; paired Student's *t* test). Furthermore, after application of ZD 7288 the resting membrane potential hyperpolarized by 10.6 ± 0.87 mV ($n = 5$, $p < 0.01$, paired Student's *t* test; Fig. 4*C*, left) and the input resistance increased by 59.4 ± 19.3 MΩ ($n = 5$, $p < 0.01$, paired Student's *t* test; Fig. 4*C*, right). These results demonstrate that the sag response and impedance profile depend upon *h* current in the bat and this current is active at resting potentials.

Layer II neurons in the Egyptian fruit bat EC exhibit a sag ratio, resonance frequency and resonance strength that all change from low in dorsal EC neurons to high in ventral EC neurons (Fig. 5*A*,*C*,*D*). In contrast, the same physiological measures in the rat changed from high in dorsal EC neurons to low in ventral EC neurons (Fig. 5*A*,*C*,*D*). In the bat, the sag activation time constant changed from slower in dorsal EC to faster in ventral EC (Fig. 5*B*), whereas in the rat the time constant changed from faster in dorsal EC to slower in ventral EC (Fig. 5*B*). Similar trends are also shown for resting membrane potential, input resistance, and membrane time constant (Fig. 5*E*–*G*). Although the sag response and resonance frequency were larger and faster in ventral EC neurons of the Egyptian fruit bat, it is important to note that there were significant differences in the means for each of these measures when compared across species. Consistent with our previous findings from the big brown bat (Heys et al., 2013), the mean resonance frequency in layer II neurons of the Egyptian fruit bat was 2.66 ± 0.31 Hz (mean ± SEM, $n = 52$), compared with 5.13 ± 0.76 Hz (mean ± SEM, $n = 24$) in the rat ($p < 0.01$, unpaired Student's *t* test). Significant differences were also found comparing the resonance strength (bat = 1.15 ± 0.02, mean ± SEM, $n = 52$; rat = 1.62 ± 0.11, mean ± SEM, $n = 24$; $p < 0.01$, unpaired Student's *t* test $p < 0.01$), sag ratio (bat = 0.18 ± 0.01, mean ± SEM, $n = 58$; rat = 0.25 ± 0.03, mean ± SEM, $n = 24$; $p < 0.025$, unpaired Student's *t* test), and sag time constant (bat = 140.05 ± 15.33 ms, mean ± SEM, $n = 58$; rat = 75.67 ± 16.71 ms, mean ± SEM, $n = 23$; $p < 0.025$, unpaired Student's *t* test). Furthermore, these differences cannot be accounted for through biased sampling of cell position (Fig. 5*L*,*M*). To compare resonance and sag response properties across both species within similar dorsal or ventral subregions of EC, the data were subdivided into recordings from neurons located in either the dorsal one-third or ventral one-third of EC (Table 1).

Discussion

The data reported here demonstrate that the intrinsic properties of neurons in layer II of the Egyptian fruit bat EC show a clear gradient of resonance frequency, resonance strength and sag ra-

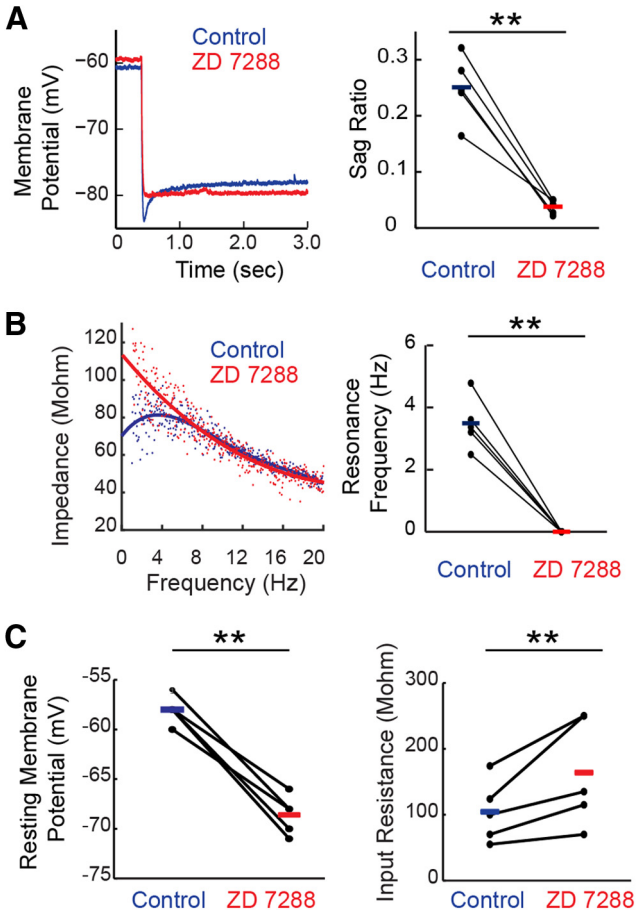

Figure 4. Sag response and impedance profile in the presence and absence of *h*-current blocker ZD 7288. ***A***, Individual neuron example (left) of the sag response measured in control ACSF (blue) and after bath application 10 μM ZD 7288 (red). Sag ratio (right) measured in five neurons in control ACSF (blue) and after bath application of 10 μM ZD 7288 (red). Blue and red bars represent mean in control (blue) and ZD 7288 (red). Asterisks represent $p < 0.01$, Paired Student's *t* test. ***B***, Individual neuron example (left) of the impedance profile measured in control ACSF (blue) and after bath application 10 μM ZD 7288 (red). Resonance frequency (right) measured in five neurons in control ACSF (blue) and after bath application of 10 μM ZD 7288 (red). Blue and red bars represent mean in control (blue) and ZD 7288 (red). ***C***, Resting membrane potential (left) before ZD 7288 (blue) and after application of 10 μM ZD 7288 (red). Input resistance (right) before ZD 7288 (blue) and after application of 10 μM ZD 7288 (red).

tio. The observed gradients are in the opposite direction of the gradients shown in the rat in our own experiments reported here and in previously published data (Giocomo et al., 2007; Giocomo and Hasselmo, 2009; Boehlen et al., 2010; Pastoll et al., 2012). Grid cells in the Egyptian fruit bat and the rat display a functional gradient characterized by an increase in grid-field spacing and grid-field size among neurons located at more ventral locations in MEC (Hafting et al., 2005; Yartsev et al., 2011; Stensola et al., 2012). In the rat, it has been suggested that this functional gradient could be generated through a physiological gradient characterized by a systematic change in *h* current time constant and *h* current amplitude expressed in layer II neurons located along the dorsal–ventral axis of MEC (Garden et al., 2008; Giocomo and Hasselmo, 2008). What then might an inverse physiological gradient between bats and rats mean in terms of mechanisms underlying the difference in grid-field spacing along the dorsal–ventral axis of MEC? One interpretation of these data could be that the *h* current-dependent gradient observed in both species may not underlie the functional gradient seen in grid-field spacing along the dorsal–ventral axis of MEC. In support of this conclusion, knock-out of HCN1 in a transgenic mouse line shows a flattening of the *h* current gradient in layer II stellate cells along the dorsal–ventral axis of MEC (Giocomo and Hasselmo, 2009), but this same knock-out does not produce a change in the slope of grid-field spacing along the dorsal–ventral axis of MEC (Giocomo et al., 2011), though it does systematically increase spacing at all dorsal–ventral positions.

It is important to note that the neurons recorded in this study are defined as layer II EC neurons based upon: (1) the position of their somata relative to the pial surface and (2) the position of their somata relative to the medial–lateral and dorsal–ventral anatomical landmarks, such as the dentate gyrus subfield of the hippocampus and the surface of the brain. The morphology and physiology observed in these neurons displayed some variability and it is possible that upon further investigation the population of layer II neurons in the Egyptian fruit bat may be able to be subdivided into multiple cell classes based upon differential electrophysiological, morphological, and/or genetic profiles. However, recording from a mixed cellular population should only reduce the appearance of a gradient observed in this study. It is possible that a physiological gradient could be generated through graded expression or by all-or-none expression within individual neurons (Fig. 6*A*). The relative lack of a smaller subpopulation of neurons located dorsally in the bat EC showing large, fast sag potential and a relative lack of a smaller subpopulation showing small, slow sag potential located more ventrally suggests that the *h*-current-dependent gradients in this study arise from graded expression of *h* current along the dorsal–ventral axis of EC. Some neurons in dorsal MEC of the Egyptian fruit bat appear to have a fan-like morphology. However, as this is the first systematic *in vitro* electrophysiological study in the EC of the Egyptian fruit bat, and only the second such study in any bat species (Heys et al., 2013), further experiments are required to build a complete picture of the physiological, morphological, and genetic profile of EC neurons. In particular, a direct measure of *h* current using voltage-clamp recordings could be done to further validate the current-clamp measurements of sag response.

The data presented here come from layer II neurons spanning the dorsal–ventral extent of the Egyptian fruit bat and the rat EC. We chose this method rather than limit the data to the dorsal–ventral extent of only the MEC to more easily compare across species, as it is difficult to accurately locate the dorsal–ventral border between MEC and lateral EC in the Egyptian fruit bat. Yet, the significant physiological gradients for the Egyptian fruit bat remain present in MEC even using a more conservative estimate of the dorsal–ventral border between medial entorhinal cortex and lateral entorhinal cortex (at 6.75 mm from the dorsal surface of the brain; Fig. 6*B–H*).

In our previous work, slice experiments were conducted using the big brown bat (*E. fuscus*; Heys et al., 2013). The intrinsic properties among layer II neurons across the two bat species showed some variation (Heys et al., 2013). In this context, the diversity of bat species, which occupy habitats spanning from desert to tropical rain forest, from mountain to river valley, in both the New and Old Worlds is worth noting. There are >1300 species of bat, and they range in mass from 1 g to several kilograms. The diets of bats vary tremendously across species, and include insects, fruits, and vertebrates, such as fish, frogs, and even other bats. Bats also differ in the extent to which they rely on vision and echolocation. For example, *R. aegyptiacus* and *E. fuscus* belong to distinct suborders of Chiroptera, inhabit separate continents, differ in mass approximately by a factor of 10, and eat fruit and insects, respectively. *R. agyptiacus* has well developed

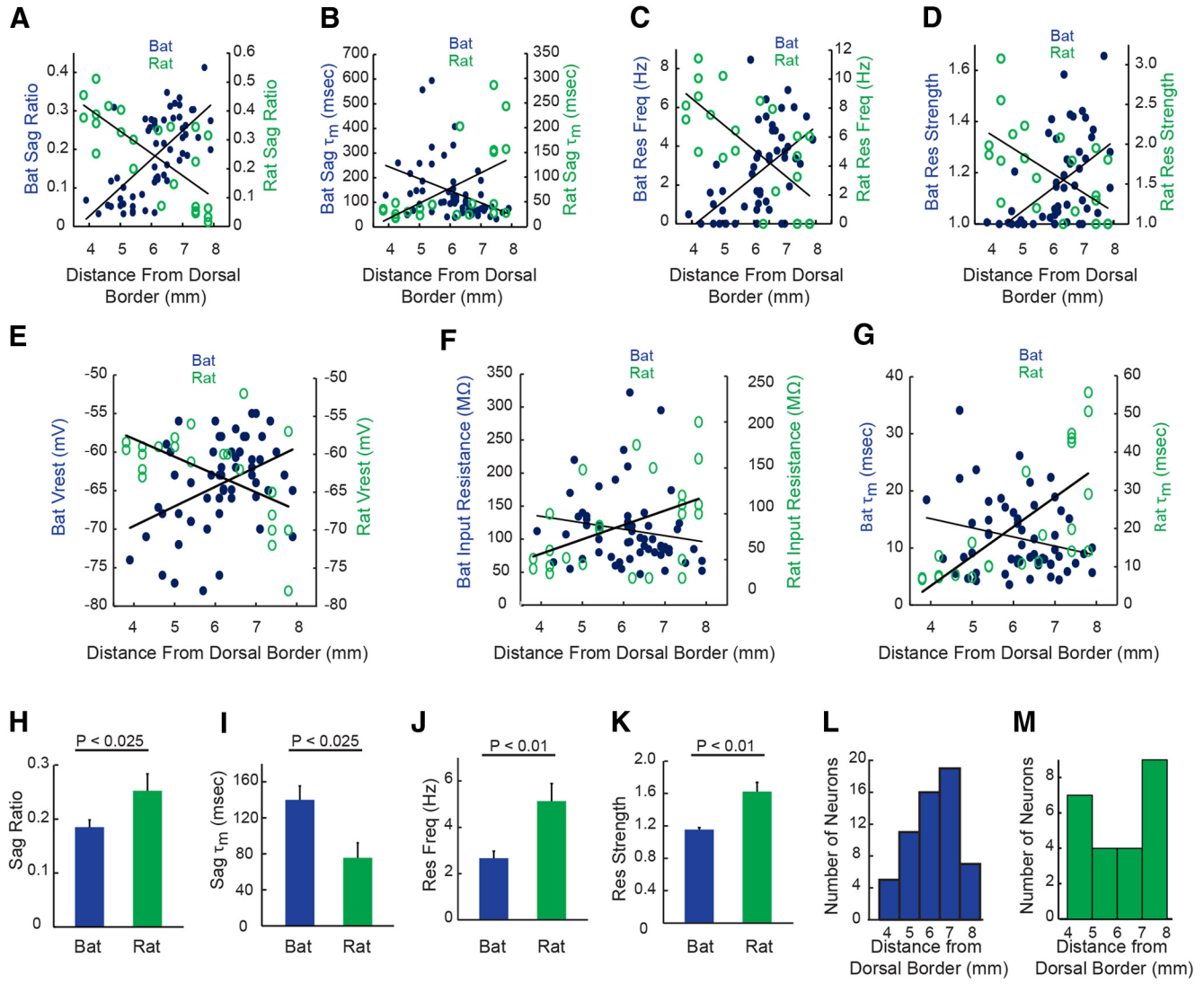

Figure 5. Bats exhibit an inverse gradient relative to rats for resonance and sag responses along the dorsal–ventral axis of EC. ***A***, Sag ratio, (***B***) sag time constant, (***C***) resonance frequency, (***D***) resonance strength, (***E***) resting membrane potential, (***F***) input resistance, and (***G***) membrane time constant input resistance, measured in bat neurons (closed blue circles) and rat neurons (open green circles) located along the dorsal–ventral axis of EC. ***H–K***, Mean sag ratio, sag time constant, resonance frequency, and resonance strength measured in bat (blue) and rat (green) neurons. Error bars depict SEM. ***L***, Histogram of bat neurons measured along the dorsal–ventral axis of EC. ***M***, Histogram of rat neurons measured along the dorsal–ventral axis of EC.

Table 1. Comparisons of bat and rat recordings restricted to the dorsal or ventral subregions of EC

	Bat	Rat	*p* value
Dorsal resonance Freq, Hz	0.71 ± 0.28 ($n = 12$)	8.11 ± 0.78 ($n = 9$)	5.35E-09
Ventral resonance Freq, Hz	3.97 ± 0.42 ($n = 19$)	2.75 ± 0.91 ($n = 11$)	0.1733
Dorsal resonance strength	1.02 ± 0.17 ($n = 12$)	2.08 ± 0.17 ($n = 9$)	8.66E-07
Ventral resonance strength	1.25 ± 0.04 ($n = 19$)	1.31 ± 0.11 ($n = 11$)	0.6109
Dorsal sag ratio	0.09 ± 0.02 ($n = 12$)	0.39 ± 0.02 ($n = 9$)	2.70E-08
Ventral sag ratio	0.27 ± 0.01 ($n = 20$)	0.15 ± 0.04 ($n = 11$)	0.0025
Dorsal sag τ, ms	187.08 ± 38.82 ($n = 12$)	29.32 ± 3.26 ($n = 9$)	2.70E-03
Ventral sag τ, ms	82.84 ± 10.74 ($n = 20$)	116.22 ± 30.51 ($n = 10$)	0.2109

Mean and SEM are shown for the dorsal one-third of EC recordings (<5.3 mm from the dorsal surface of the brain in the bat and <5.2 mm from the dorsal surface of the brain in the rat) and for the ventral one-third of EC recordings (>6.5 mm from the dorsal surface of the brain in the bat and >6.4 mm from the dorsal surface of the brain in the rat). *p* values are shown for unpaired Student's *t* test.

vision and a rudimentary form of lingual echolocation, which it uses to find large objects and avoid obstacles under low-light conditions. By contrast, *E. fuscus* has comparatively poor vision and a high-resolution laryngeal echolocation system, which it uses to hunt insect prey on the wing (Fenton and Simmons, 2015). The differences between layer II neuron intrinsic properties in *Eptesicus* and *Rousettus* points to the need for future research to investigate the relative contributions of brain size, circuitry, and/or dependence on sensing modalities to species differences in single-cell physiology.

Although our data demonstrate that intrinsic cellular electrophysiological properties in the Egyptian fruit bat and the rat display inverse relationships along the dorsal–ventral axis of EC, it is worth noting that the sag response properties and the resonance

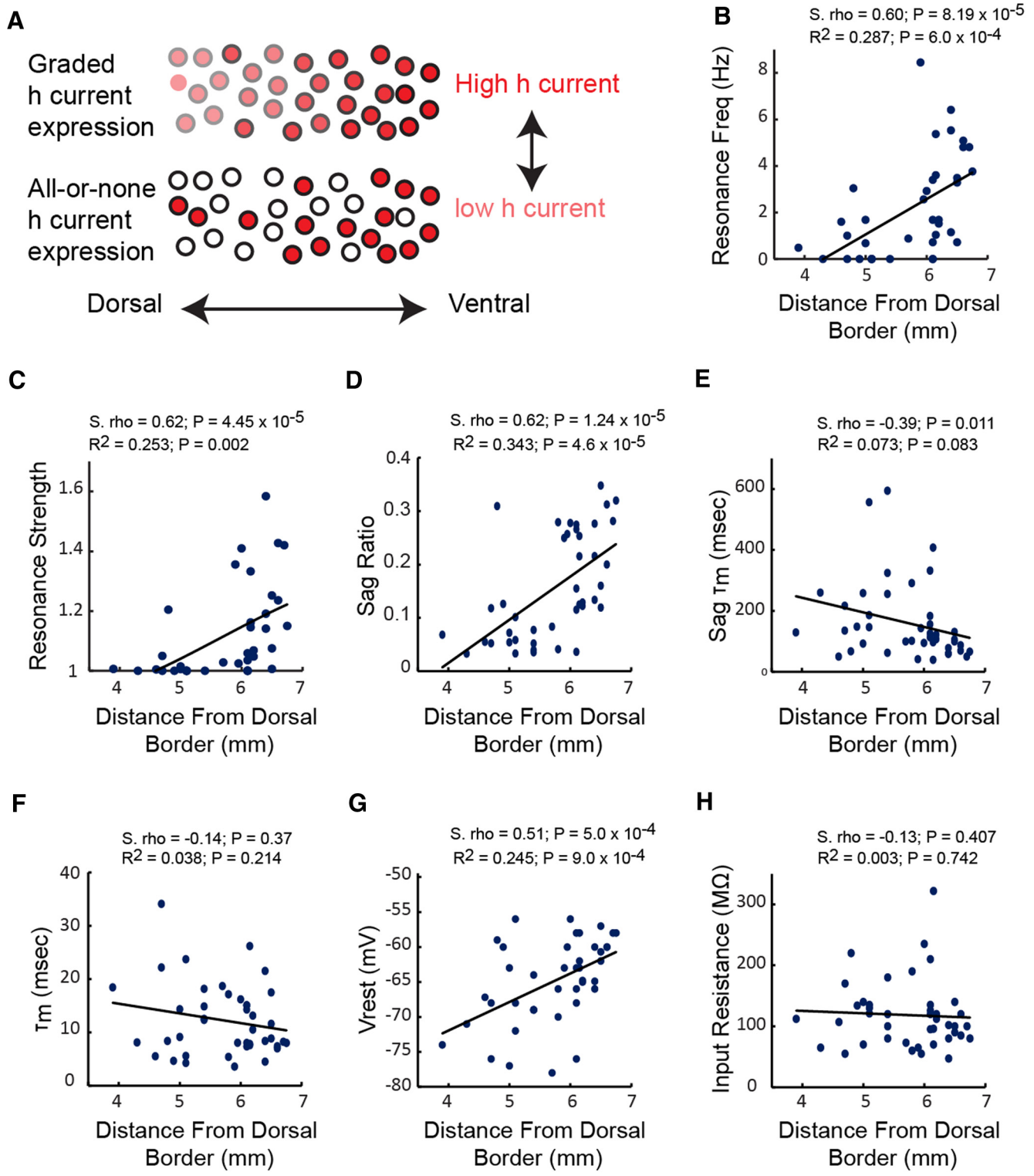

Figure 6. Possible cellular *h* current expression patterns along the dorsal–ventral axis of EC. ***A***, A gradient in *h*-current-dependent properties, such as sag ratio, sag time constant, resonance frequency, or resonance strength, observed across a population of neurons, could arise from: (1) a graded patterns of *h* current expression (top), or (2) an all-or-none pattern of expression (bottom). ***B***, Resonance frequency, (***C***) resonance strength, (***D***) sag ratio, (***E***) sag time constant, (***F***) membrane time constant, (***G***) resting membrane potential, (***H***) input resistance, and (***G***) input resistance measured across the dorsal–ventral extent of MEC, using conservative estimates of the dorsal–ventral border between MEC and lateral EC (LEC; ie, <6.75 mm from the dorsal surface of the brain). Rho and *p* values for the Spearman rank test (S. rho), and R^2 with their *p* values for the linear fits, are shown above for each plot.

response properties in both species are dependent upon *h* current. These results, along with previously published recordings from grid cells in HCN1 knock-out mice (Giocomo et al., 2011), suggest that the *h* current may not underlie the functional gradient seen in grid-field spacing along the dorsal–ventral axis of MEC (Hafting et al., 2005). Experiments conducted using *in vitro* slice preparations have attributed *h* current expression to a range of neuronal function including synaptic normalization and

synaptic integration, control of the spike threshold and resting membrane potential, as well as influencing the time course of afterhyperpolarization potentials (Magee, 1999; Nolan et al., 2004, 2007; Otmakhova and Lisman, 2004; Garden et al., 2008; Dudman and Nolan, 2009). Beyond the potential role of *h* current in determining the resonance of neurons, the *h* current could influence the firing properties of grid cells, such as size and spacing via a different mechanism, such as regulating the temporal summation of synaptic input and thereby influencing the induction of LTP (Nolan et al., 2007; Garden et al., 2008; Dudman and Nolan, 2009; Mehta, 2011). Furthermore, recent anatomical studies have shown that the EC displays an inverse relationship of calbindin expression and corresponding cholinergic innervation between rodents and bat (Naumann et al., 2016).

It is also worth noting that grid cells at different dorsal to ventral positions in rats have been shown to have different responses to changes in visual features (Stensola et al., 2012), and this has been modeled as a difference in sensitivity of grid cells at different dorsal to ventral anatomical locations to stimulation patterns from different portions of the visual field (Raudies and Hasselmo, 2015). Our reported species differences in EC gradients might be related to differences in optic flow experienced by flying bats and running rats. As such, these observations should help to guide further experiments aimed at determining the functional role of *h* current in the context of MEC function and grid-cell firing properties.

References

Alonso A, Klink R (1993) Differential electroresponsiveness of stellate and pyramidal-like cells of medial entorhinal cortex layer II. J Neurophysiol 70:128–143. Medline

Alonso A, Llinás RR (1989) Subthreshold Na+-dependent theta-like rhythmicity in stellate cells of entorhinal cortex layer II. Nature 342:175–177. CrossRef Medline

Boehlen A, Heinemann U, Erchova I (2010) The range of intrinsic frequencies represented by medial entorhinal cortex stellate cells extends with age. J Neurosci 30:4585–4589. CrossRef Medline

Dickson CT, Magistretti J, Shalinsky MH, Fransén E, Hasselmo ME, Alonso A (2000) Properties and role of I_h in the pacing of subthreshold oscillations in entorhinal cortex layer II neurons. J Neurophysiol 83:2562–2579. Medline

Doeller CF, Barry C, Burgess N (2010) Evidence for grid cells in a human memory network. Nature 463:657–661. CrossRef Medline

Dudman JT, Nolan MF (2009) Stochastically gating ion channels enable patterned spike firing through activity-dependent modulation of spike probability. PLoS Comput Biol 5:e1000290. CrossRef Medline

Erchova I, Kreck G, Heinemann U, Herz AV (2004) Dynamics of rat entorhinal cortex layer II and III cells: characteristics of membrane potential resonance at rest predict oscillation properties near threshold. J Physiol 560:89–110. CrossRef Medline

Fenton BM, Simmons NB (2015) A world of science and mystery. Chicago: University of Chicago.

Fyhn M, Molden S, Witter MP, Moser EI, Moser MB (2004) Spatial representation in the entorhinal cortex. Science 305:1258–1264. CrossRef Medline

Fyhn M, Hafting T, Witter MP, Moser EI, Moser MB (2008) Grid cells in mice. Hippocampus 18:1230–1238. CrossRef Medline

Garden DL, Dodson PD, O'Donnell C, White MD, Nolan MF (2008) Tuning of synaptic integration in the medial entorhinal cortex to the organization of grid cell firing fields. Neuron 60:875–889. CrossRef Medline

Giocomo LM, Hasselmo ME (2008) Time constants of *h* current in layer ii stellate cells differ along the dorsal to ventral axis of medial entorhinal cortex. J Neurosci 28:9414–9425. CrossRef Medline

Giocomo LM, Hasselmo ME (2009) Knock-out of HCN1 subunit flattens dorsal-ventral frequency gradient of medial entorhinal neurons in adult mice. J Neurosci 29:7625–7630. CrossRef Medline

Giocomo LM, Zilli EA, Fransén E, Hasselmo ME (2007) Temporal frequency of subthreshold oscillations scales with entorhinal grid cell field spacing. Science 315:1719–1722. CrossRef Medline

Giocomo LM, Hussaini SA, Zheng F, Kandel ER, Moser MB, Moser EI (2011) Grid cells use HCN1 channels for spatial scaling. Cell 147:1159–1170. CrossRef Medline

Hafting T, Fyhn M, Molden S, Moser MB, Moser EI (2005) Microstructure of a spatial map in the entorhinal cortex. Nature 436:801–806. CrossRef Medline

Heys JG, MacLeod KM, Moss CF, Hasselmo ME (2013) Bat and rat neurons differ in theta-frequency resonance despite similar coding of space. Science 340:363–367. CrossRef Medline

Jacobs J, Weidemann CT, Miller JF, Solway A, Burke JF, Wei XX, Suthana N, Sperling MR, Sharan AD, Fried I, Kahana MJ (2013) Direct recordings of grid-like neuronal activity in human spatial navigation. Nat Neurosci 16:1188–1190. CrossRef Medline

Killian NJ, Jutras MJ, Buffalo EA (2012) A map of visual space in the primate entorhinal cortex. Nature 491:761–764. CrossRef Medline

Klink R, Alonso A (1997) Morphological characteristics of layer II projection neurons in the rat medial entorhinal cortex. Hippocampus 7:571–583. CrossRef Medline

MacLeod KM, Horiuchi TK, Carr CE (2007) A role for short-term synaptic facilitation and depression in the processing of intensity information in the auditory brain stem. J Neurophysiol 97:2863–2874. CrossRef Medline

Magee JC (1999) Dendritic I_h normalizes temporal summation in hippocampal CA1 neurons. Nat Neurosci 2:508–514. CrossRef Medline

Mehta MR (2011) Contribution of Ih to LTP, place cells, and grid cells. Cell 147:968–970. CrossRef Medline

Naumann RK, Ray S, Prokop S, Las L, Heppner FL, Brecht M (2016) Conserved size and periodicity of pyramidal patches in layer 2 of medial/caudal entorhinal cortex. J Comp Neurol 524:783–806. CrossRef Medline

Nolan MF, Malleret G, Dudman JT, Buhl DL, Santoro B, Gibbs E, Vronskaya S, Buzsáki G, Siegelbaum SA, Kandel ER, Morozov A (2004) A behavioral role for dendritic integration: HCN1 channels constrain spatial memory and plasticity at inputs to distal dendrites of CA1 pyramidal neurons. Cell 119:719–732. CrossRef Medline

Nolan MF, Dudman JT, Dodson PD, Santoro B (2007) HCN1 channels control resting and active integrative properties of stellate cells from layer II of the entorhinal cortex. J Neurosci 27:12440–12451. CrossRef Medline

Noll UG (1979) Body temperature, oxygen consumption, noradrenaline response and cardiovascular adaptations in the flying fox, *Rousettus aegyptiacus*. Comp Biochem Physiol 63:79–88. CrossRef

Otmakhova NA, Lisman JE (2004) Contribution of I_h and GABAB to synaptically induced afterhyperpolarizations in CA1: a brake on the NMDA response. J Neurophysiol 92:2027–2039. CrossRef Medline

Pastoll H, Ramsden HL, Nolan MF (2012) Intrinsic electrophysiological properties of entorhinal cortex stellate cells and their contribution to grid cell firing fields. Front Neural Circuits 6:17. CrossRef Medline

Raudies F, Hasselmo ME (2015) Differences in visual-spatial input may underlie different compression properties of firing fields for grid cell modules in medial entorhinal cortex. PLOS Comput Biol 11:e1004596. CrossRef Medline

Shay CF, Boardman IS, James NM, Hasselmo ME (2012) Voltage dependence of subthreshold resonance frequency in layer II of medial entorhinal cortex. Hippocampus 22:1733–1749. CrossRef Medline

Stensola H, Stensola T, Solstad T, Frøland K, Moser MB, Moser EI (2012) The entorhinal grid map is discretized. Nature 492:72–78. CrossRef Medline

Ting JT, Daigle TL, Chen Q, Feng G (2014) Acute brain slice methods for adult and aging animals: application of targeted patch clamp analysis and optogenetics. Methods Mol Biol 1183:221–42 CrossRef Medline

Yartsev MM, Witter MP, Ulanovsky N (2011) Grid cells without theta oscillations in the entorhinal cortex of bats. Nature 479:103–107. CrossRef Medline